Analytical calculation of temperature-induced strain of supertall structures

Fei Gao[1], Pan Chen[2], Shun Weng[3*], Yong Xia[4], Hongping Zhu[5]

Abstract: Estimating temperature-induced strain is of critical importance for structural safety assessment. Most previous studies estimated the temperature-induced strain by statistical analysis, resulting in the unexplainable physical meaning of the obtained model coefficients. In this paper, an analytical formula for the temperature-induced strain of supertall structures is derived based on the simulated temperature field. First, a supertall structure is simplified as a cantilever column and the theoretical relationship between the sectional two-dimensional temperature field and strain is derived. Afterwards, the structure is extended to a generalised cantilever column bounded by springs at the top end, and the theoretical relationship of temperature and strain is derived as well. The formula shows that the sectional strain is composed of the sectional average temperature-induced strain and the gradient temperature-induced strain along two horizontal directions. A finite element (FE) model is established to verify the derived strain formula. Finally, the formula is applied to a real supertall structure, the Wuhan Yangtze River Navigation Centre, on which a long-term structural health monitoring system has been installed. The temperature field of the whole structure is obtained by the FE heat transfer analysis, and the temperature-induced strain is calculated according to the derived formula. The average difference between the theoretically derived and the measured strain is less than 7 με. This study provides a simple theoretical formula for calculating the temperature-induced strain of supertall structures, avoiding the complicated FE structural analysis.

Keywords: supertall structures, temperature-induced strain, field monitoring, thermal action, theoretical formula

---

[1] Professor, School of Civil and Hydraulic Engineering, Huazhong University of Science and Technology, Wuhan, Hubei, P.R. China.

[2] PhD Student, School of Civil and Hydraulic Engineering, Huazhong University of Science and Technology, Wuhan, Hubei, P.R. China.

[3] Professor, School of Civil and Hydraulic Engineering, Huazhong University of Science and Technology, Wuhan, Hubei, P.R. China. (Corresponding author). E-mail: wengshun@hust.edu.cn

[4] Professor, Department of Civil and Environmental Engineering, The Hong Kong Polytechnic University, Hong Kong, P.R. China.

[5] Professor, School of Civil and Hydraulic Engineering, Huazhong University of Science and Technology, Wuhan, Hubei, P.R. China.

1. Introduction

Structural health monitoring (SHM) has been widely deployed in large-scaled civil structures for evaluating their safety conditions [1–3]. The collected data from the SHM system not only measure the real structural response but also, more importantly, the static response caused by the environment [4, 5]. Variations in temperature-induced responses may mask the damage-induced response, which eventually results in erroneous evaluations. In recent years, a large number of supertall structures have installed SHM systems for performance evaluation [6–11]. The periodic fluctuation of temperature is the direct cause of changes in structural strain and displacement. However, research on estimating the temperature effect of supertall structures remains insufficient.

Early supertall SHM projects mostly focused on a single aspect of structural deformation, building top displacement and acceleration whereas rarely considered the temperature effect [12–14]. Recently, scholars have gradually realised that the temperature effect on structures cannot be ignored. Tamura et al. [15] unexpectedly found that thermal stress could cause a 4-cm top displacement when they measured the wind-induced response of a building by using RTK-GPS. Breuer et al. [16] studied the effects of solar radiation and temperature changes on the horizontal displacement of the top of the Stuttgart TV tower. The results showed that the daily movement trajectory of the tower top was related to the periodic changes in sunlight and atmospheric temperature. Xia et al. [17] derived the horizontal displacement and inclination of the 600 m tall Canton Tower by using multi-sectional strain data. They [18, 19] comprehensively studied the temperature distribution and the associated action of the Canton Tower. The movement of the tower top on a sunny day in winter was 15.7 cm in the east–west direction and 15.5 cm in the north–south. From summer to winter, the entire tower tilted toward northeast with the horizontal movement of 15 cm approximately at the tower top. Su et al. [20] also separated the typhoon- and temperature-induced quasi-static responses of the structure and found that the former was less than the latter.

Strain is an important static response parameter of a structure and closely related to its stress and displacement. The measured strain comes from various sources such as dead load, live load, winds, temperature, concrete shrinkage, concrete creep and other loads. Among these factors, concrete shrinkage and creep mainly occur at the initial stage of construction and gradually decrease with time. Temperature-induced strain exhibits a daily, seasonal and annual variation pattern. A number of studies have found that environment temperature-induced strain is more significant than other load-induced (Zhu et al. [21]). Moreover, the temperature field of a structure is generally non-uniform, causing the variations in the strain and temperature not synchronised (Yang et al. [22]). Therefore, the strain is related to the overall temperature field of the entire structure, not a single temperature point, which leads to the complicated relation between the strain and temperature.

Obtaining the temperature field of the entire structure and calculating the temperature-induced response are two key steps for studying the temperature effect. FE heat transfer analysis has been developed for calculating the temperature field. Ni et al. [23] combined on-site monitoring data and FE heat transfer analysis to establish a temperature field model inside the concrete, which provided reliable input for the numerical simulation of temperature-induced deformation and internal forces. Su [24] calculated the temperature field of a single component of Canton Tower. By assuming the temperature field of the structure along the height is uniform, the temperature-induced deformation under several typical cases were calculated by manually inputting the temperature load. This divide-and-conquer approach is inefficient and cannot achieve real-time safety assessment. Gao et al. [25] proposed an efficient method for calculating the overall temperature field of a supertall structure. By establishing a virtual sun, the dynamic thermal boundary conditions under solar radiation were established and the dynamic temperature field of the whole structure was accurately simulated. In these heat transfer analyses, the steel bars were not modelled as the steel bars inside the concrete have negligible effects on the overall temperature field. However, in the structural FE analysis, the steel bars should be modelled as the contribution of steel bars to the sectional stiffness is larger. Including the steel bars will generate numerous elements, which is time-consuming for a large-scale supertall structure [25].

Statistical analysis is another method to estimate the relation between temperature and structural response. Hu et al. [26] have studied the quantitative relationship between displacement and multiple temperature of the Canton Tower in different seasons based on linear regression analysis. The results showed that a regularized linear regression model was able to describe the physical relationship between the temperature and displacement whereas an ordinary linear regression model could not. Bai et al. [27, 28] established the relationship between the strain and the temperature of a typical Tibetan timber building from 2-year monitoring data by combining singular spectrum analysis and polynomial regression. The disadvantages of the statistical analyses include the dependence on the accuracy of the measured data and the unexplainable physical meaning of model coefficients. Additionally, the statistical analysis predicts the structural response through the previous response data and relies on the authenticity of such data. This response–response mapping is prone to systematic deviations. For example, if the previous strain data includes structural damage, the established quantitative relationship between temperature and strain also includes structural damage and thus cannot reflect the original mechanical relationship between temperature and strain.

In a word, a simpler and more efficient method is needed to calculate the temperature-induced response, especially the temperature-induced strain. This paper derives the theoretical temperature-strain formula for supertall structures and thus the complex mapping relationship between temperature and structural response is realized. The framework of this paper is as follows. Firstly, the virtual sun method for calculating time-varying temperature field is briefly described. Secondly, the theoretical temperature-strain formula of the cantilever and generalised cantilever columns is derived. Thirdly, an FE column model verifies the correctness of the formula. Finally, the temperature-strain formula is applied to calculate the temperature-induced strain of the 335 m tall Wuhan Yangtze River Navigation Centre.

2. Time-varying temperature field calculation by virtual sun method

2.1. Determination of the relative position of the sun

The relative position of the sun (Fig. 1) can be determined by solar altitude angle β, solar azimuth angle α and the distance of the sun from the earth d. The distance d is treated as a constant given that its variation in one year is small. The solar altitude angle β and solar azimuth angle α are derived in [25] and expressed as

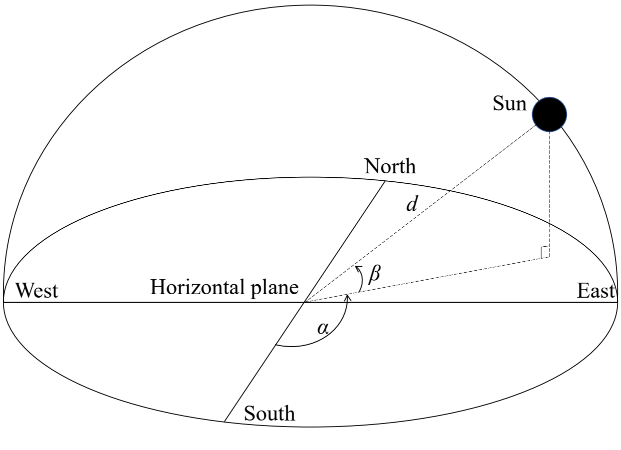

Fig. 1. Relative position of the sun

$$\beta = \arcsin\left\{ \sin\varphi \sin[23.5\sin(\frac{\tau}{365})] + \cos\varphi \cos[23.5\sin(\frac{\tau}{365})]\cos\tau \right\}, \tag{1}$$

$$\alpha = \begin{cases} 360 - \arccos\left\{ \dfrac{\sin\beta\sin\varphi - \sin[23.5\sin(\frac{\tau}{365})]}{\cos\beta\cos\varphi} \right\}, 360m < \tau \le 360m + 180 \\ \arccos\left\{ \dfrac{\sin\beta\sin\varphi - \sin[23.5\sin(\frac{\tau}{365})]}{\cos\beta\cos\varphi} \right\}, 360m + 180 < \tau \le 360m + 360 \end{cases}, \tag{2}$$

where φ represents latitude, and τ is the radiation calendar angle. In the radiation calendar system, March 21 (vernal equinox) 0:00:00 is set as the reference with τ increasing by 15° per hour and changes from 0° to 131400°; m= 0, 1, 2, …, 364.

2.2. Heat transfer equations and boundary conditions

According to the Fourier heat transfer theorem and the energy conservation theorem, the governing equation for heat transfer problems can be established as [29]

$$\rho c\frac{\partial T}{\partial t}=k_x\frac{\partial^2 T}{\partial x^2}+k_y\frac{\partial^2 T}{\partial y^2}+k_z\frac{\partial^2 T}{\partial z^2}, \tag{3}$$

where x, y and z are the Cartesian coordinates; ρ (kg/m^3) is the density of the material; c (J/(kg·°C)) represents the specific heat coefficient; T (°C) represents the temperature at coordinate point (x, y, z) and k_x, k_y and k_z (W/(m·°C)) is the thermal conductivity coefficients of different directions.

The thermal initial and boundary conditions are required for solving Eq. (3). The thermal initial condition is the end-time temperature field in the previous analysis, which can be set as a uniform temperature field. The thermal boundary condition is determined by the following equations [30]

$$(h_c+h_r)(T_a+\frac{\alpha_s I}{h_c+h_r}-T)+k\frac{\partial T}{\partial n}=0, \tag{4}$$

$$h_c+h_r=9.8+3.8v, \tag{5}$$

where h_c (W/(m^2·°C)) is the convective coefficient between the structural surface and the atmosphere; h_r (W/(m^2·°C)) is the radiant heat transfer coefficient; h_c and h_r are in correlation with average wind velocity v, which is simplified as Eq. (5); T_a (°C) represents the environmental temperature; α_s ($0 < \alpha_s < 1$) is the absorptivity coefficient of the surface; I (W/m^2) is the intensity of the solar radiation projected onto the surface; k (W/(m·°C)) represents the thermal conductivity coefficient and is assumed identical in three directions and n is the normal direction of the surface.

When applying the thermal boundary conditions, the irradiation elements receive solar radiation, whereas the shade elements receive none. The irradiation and shade elements are distinguished by the hemicube method [31]. A virtual sun, determined by Eq. (1) and (2) is established in the FE model. The sun is treated as a radiation source, while the structural elements are treated as absorbers. The angle coefficient between the radiation source and the absorbers are calculated. If the angle coefficient is not equal to zero, then the radiation source can 'see' the absorber, which is defined as the irradiation element. Otherwise, the radiation source cannot 'see' the absorption element and is referred to as the shade element. The value of the angle coefficient is used to distinguish the shade and irradiation elements automatically [25].

3. Derivation of temperature-strain formulas for supertall structures

After obtaining the whole temperature field of the structure, a structural FE model is generally established for calculating the temperature-induced response. Because the steel bars contribute a lot to the sectional stiffness, the structural FE model needs to build a large number of steel bar elements, which results in long calculation time and low calculation accuracy. In order to avoid this disadvantage, this paper will develop another method that can calculate the structural response without establishing a structural FE model. Considering that the deformation profile of the whole structure caused by solar radiation is the first bending mode [17], the supertall structure is equivalent to a multi-story and variable sectional cantilever column model (Fig. 2 (b)). In the model: the bottom is fully constrained; the core tube and the columns are connected by beams and slabs; the cross section of the core tube decreases linearly from the bottom to top. Under the effect of ambient temperature, the non-uniform temperature of the outer columns change significantly, resulting in greater strain variations than the core tube. Therefore, we will focus on the temperature-induced strain of the outer columns. For a column on each floor, its temperature-induced strain is independent of the strain of the upper and lower columns. It can be equivalent to a generalised cantilever column (Fig. 2 (c)), which is fully constrained at the bottom and constrained with axial and rotation springs at the top. The temperature-induced strain of a column is only related to the sectional temperature field. Firstly, the analytical calculation of the temperature-induced strain for the cantilever column is derived, and then extended to the generalised cantilever column. This paper extends the traditional single-point temperature-strain formula (i.e., $\Delta\varepsilon = \alpha\Delta T$) to the sectional temperature field-strain formula for calculating the temperature-induced strain. Consequently, establishing a structural FE model is avoided.

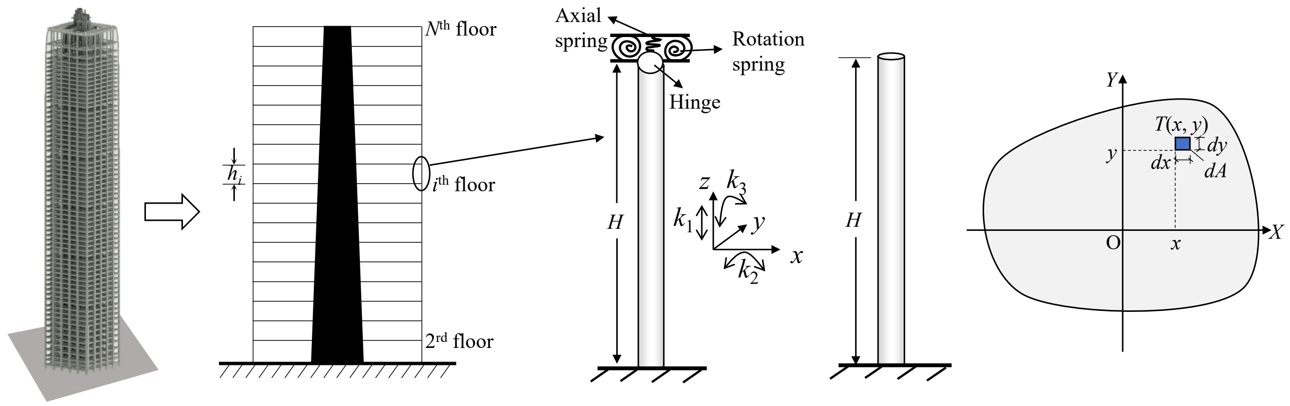

(a) Supertall structure (b) Multi-story and variable sectional cantilever column model (c) Generalized cantilever column model (d) Cantilever column model (e) Sectional temperature field $T(x, y)$

Fig. 2. Theoretical model

3.1. Cantilever column model

As shown in Fig. 2 (d), the cantilever column has a height of *H*, and the bottom is fully constrained. Assume that the sectional temperature field at the initial time is constant 0, and at a certain time is *T*(*x*, *y*). Firstly, we completely constrain the top of the column so that the column does not deform. The stress at any point (*x*, *y*) in the section due to the temperature change is $\sigma(x,y)=E\alpha T(x,y)$, where *E* represents the elastic modulus and *α* is thermal expansion coefficient. At this time, the axial force to be applied at the top can be expressed as $F_N=\int\sigma(x,y)dA=\int E\alpha T(x,y)dA$. In addition to the axial force, the non-uniform distributed stress in the cross section also generates bending moments. The bending moments along the x- and y-axis are $M_x=\int E\alpha T(x,y)ydA$, $M_y=\int E\alpha T(x,y)xdA$.

Next the constraints at the top are released. We need to apply external forces of F'_N, M'_x and M'_y to make the cantilever column the same as the initial state. Assuming that the deformation of the section meets the plane section assumption, the strain caused by the axial force and bending moment at any point (x_0, y_0) are respectively: $\varepsilon'_0=\frac{F_N}{EA}=\frac{\alpha\int T(x,y)dA}{A}$, $\varepsilon'_m=\frac{M_x}{EI_x}y_0+\frac{M_y}{EI_y}x_0$, where ε'_0 and ε'_m refer to the *z*-direction strains, I_x and I_y are moments of inertia with respect to the *x*- and *y*-axis, respectively. The total strain at any coordinate (x_0, y_0) is summed as

$$\varepsilon'=\varepsilon'_0+\varepsilon'_m=\frac{\alpha\int T(x,y)dA}{A}+\frac{\alpha\int T(x,y)ydA}{I_x}y_0+\frac{\alpha\int T(x,y)xdA}{I_y}x_0\,. \tag{6}$$

If take $T'_A=\frac{\int T(x,y)dA}{A}$, $T'_{ex}=\frac{\int T(x,y)ydA}{I_x}$, $T'_{ey}=\frac{\int T(x,y)xdA}{I_y}$, then,

$$\varepsilon'(x_0,y_0)=\alpha(T'_A+T'_{ex}\cdot y_0+T'_{ey}\cdot x_0)\,. \tag{7}$$

The above formula shows the relationship between the strain and the sectional temperature field at arbitrary coordinates. T'_A can be regarded as the sectional average temperature, and T'_{ex}, T'_{ey} can be regarded as the gradient temperature along the *x*-axis and *y*-axis directions, respectively. When the temperature remains constant along the *y* direction, then $T'_{ex}=0$. So does T'_{ey}. At any time, when the sectional temperature field is known, T'_A, T'_{ex} and T'_{ey} are all available. The strain of any point can then be calculated from the coordinates and the sectional temperature field.

3.2. Generalised cantilever column model

The generalised cantilever column model is shown in Fig. 2 (c). The constraints of beams and slabs on the column are equivalent with axial and rotation springs at the top. The top axial spring stiffness, *x*- and *y*-rotation spring stiffness are k_1, k_2, and k_3, respectively. A similar process is used to derive the temperature-strain formula under the temperature field $T\,(x, y)$.

The axial displacement at the column top is defined as generalised displacements u_0. The *x*- and *y*-rotation angles at the top are defined as generalised rotation angles θ_x and θ_y, respectively. When the top is unconstrained, the equivalent force caused by the temperature field $T\,(x, y)$ is calculated as $F_N = \int E\alpha T(x,y)dA$, $M_x = \int E\alpha T(x,y)ydA$, and $M_y = \int E\alpha T(x,y)xdA$. The top springs will constrain the top displacement. The constrained displacement will produce internal forces. The equilibrium equation between the internal and external forces requires that, $F_N - k_1u_0 = \frac{u_0}{H}EA$, $M_x - k_2\theta_x = EI_x\delta_x''$, $M_y - k_3\theta_y = EI_y\delta_y''$, where δ_x and δ_y represent the lateral displacement at the top along the *x*- and y-directions, respectively.

Consider the relationship between the top lateral displacement and the rotation. The expressions of M_x and M_y show that the bending moments M_x and M_y are directly caused by the temperature field $T(x, y)$. Thus, M_x and M_y remain constant along the height direction. As the first derivative of the lateral displacement is the rotation and the first derivative of the rotation is proportional to the bending moment, the rotation is a linear function of height and the lateral displacement is a quadratic function of height. Moreover, the *x*-direction rotation angles at the bottom and top are 0 and θ_x, respectively. Then, the rotation equation at an arbitrary height z is expressed by $\delta_x'(z) = 0 + \frac{\theta_x - 0}{H}z = \frac{\theta_x}{H}z$. According to $\delta_x'(z)$, we get $\delta_x''(z) = \frac{\theta_x}{H}$. $\delta_x''(z)$ shows that the $\delta_x''(z)$ remains constant in the height direction. When substitute $\delta_x''(z)$ into $M_x - k_2\theta_x = EI_x\delta_x''$ and then have $k_2 = \frac{M_x}{\theta_x} - \frac{EI_x}{H}$. k_3 can be calculated in a similar manner. Therefore, k_1, k_2 and k_3 are expressed as

$$k_1 = \frac{F_N}{u_0} - \frac{EA}{H}, \tag{8}$$

$$k_2 = \frac{M_x}{\theta_x} - \frac{EI_x}{H}, \tag{9}$$

$$k_3 = \frac{M_y}{\theta_y} - \frac{EI_y}{H}. \tag{10}$$

k_1, k_2 and k_3 are stiffness and can be regarded as constants. The relationship between the generalised displacement and temperature can be derived from Eqs. (8) to (10): $u_0 = \dfrac{F_N}{k_1 + \dfrac{EA}{H}}$, $\theta_x = \dfrac{M_x}{k_2 + \dfrac{EI_x}{H}}$, $\theta_y = \dfrac{M_y}{k_3 + \dfrac{EI_y}{H}}$. According to the plane section assumption, the strain in the section is linearly distributed, $\varepsilon = \dfrac{u_0}{H} + \dfrac{\theta_x}{H} y + \dfrac{\theta_y}{H} x$. Take the obtained u_0, θ_x and θ_y into $\varepsilon = \dfrac{u_0}{H} + \dfrac{\theta_x}{H} y + \dfrac{\theta_y}{H} x$, we get $\varepsilon = \dfrac{F_N}{k_1 H + EA} + \dfrac{M_x}{k_2 H + EI_x} y + \dfrac{M_y}{k_3 H + EI_y} x$. Since F_N, M_x and M_y are functions of the temperature field $T(x, y)$, the strain at any point (x_0, y_0) can be obtained as

$$\varepsilon = \alpha \left(\frac{\int T(x,y) dA}{\frac{k_1 H}{E} + A} + \frac{\int T(x,y) y dA}{\frac{k_2 H}{E} + I_x} y_0 + \frac{\int T(x,y) x dA}{\frac{k_3 H}{E} + I_y} x_0 \right). \tag{11}$$

Let

$$T_A = \frac{\int T(x,y) dA}{\frac{k_1 H}{E} + A}, \quad T_{ex} = \frac{\int T(x,y) y dA}{\frac{k_2 H}{E} + I_x}, \quad T_{ey} = \frac{\int T(x,y) x dA}{\frac{k_3 H}{E} + I_y}, \tag{12}$$

then,

$$\varepsilon(x_0, y_0) = \alpha (T_A + T_{ex} \cdot y_0 + T_{ey} \cdot x_0). \tag{13}$$

It is noteworthy that Eq. (11) and (6) are similar and Eq. (11) degenerates into Eq. (6) as $k_1 = k_2 = k_3 = 0$. Therefore Eq. (11) is more general.

Eq. (13) shows that the strain occurs within a three-dimensional plane and consists of three components: the sectional axial deformation caused by T_A, y-direction deviation deformation by T_{ex} and x-direction deviation deformation by T_{ey}.

4. Formula verification by an FE model

In this section, a generalised cantilever column model subjected only to temperature loads will be established. Based on the simulated temperature field, the temperature-induced strain is calculated from Eq. (11) and then compared with the strain calculated by the FE thermal-structure coupling analysis.

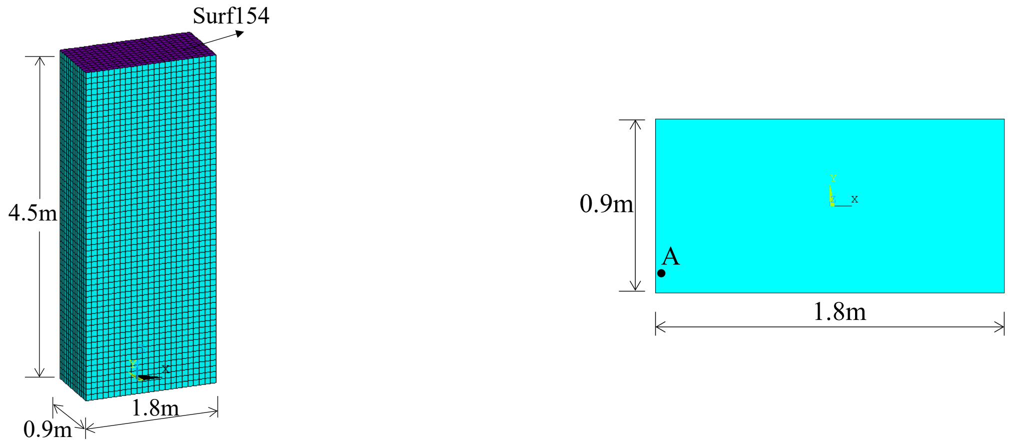

(a) FE model (b) A section

Fig. 3. Generalized cantilever column model

Table 1. Material parameters used in generalized cantilever column FE model

Density /(kg/m^3)	Elastic modulus /(N/m^2)	Poisson's ratio	Thermal expansion coefficient /°C^{-1}	Thermal conductivity /W/(m·°C)	Specific heat coefficient /(J/(kg·°C)
2635	3.7×10^{10}	0.28	10×10^{-6}	2.33	921

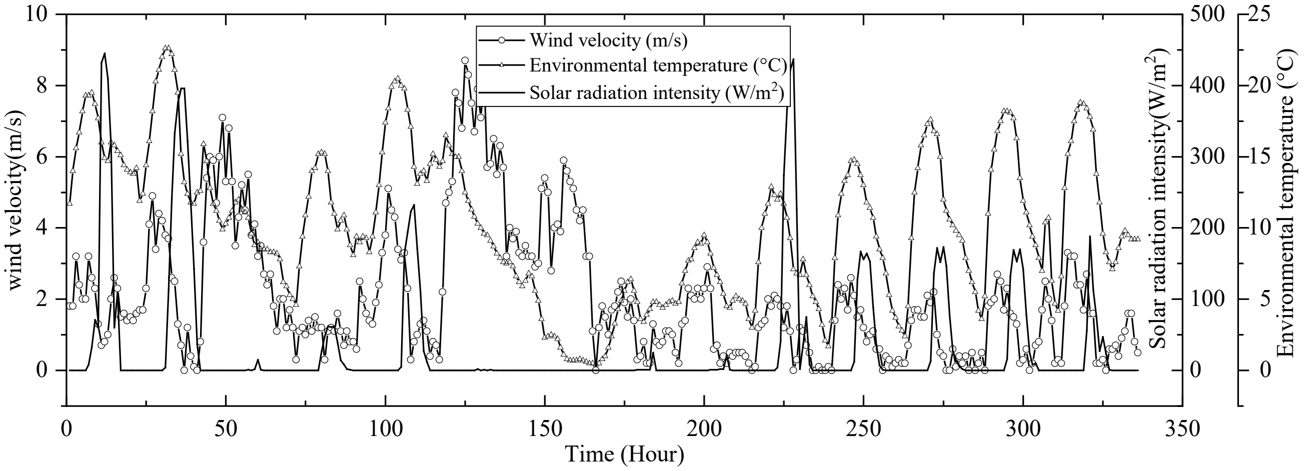

Fig. 4. Meteorological data

As shown in Fig. 3, the generalised cantilever model is in a rectangular cross section with the dimensions of 0.9 m × 1.8 m × 4.5 m. The column is constrained by axial and rotation springs at the top and fully constrained at the bottom. These springs are added by applying surface effect elements SURF154 in ANSYS. The surface effect elements are attached to the top surface of the model for simulating the axial and rotation springs. The stiffness of the axial and rotation springs are time-independent, which are calculated according to Eqs. (8) to (10). k_1, k_2 and k_3 are 1.33×10^{10} N/m, 8.92×10^8 N·m and 3.58×10^9 N·m, respectively. The element mesh size is set as 80 mm. The material parameters of this model are shown in Table 1. Meteorological data from weather station (Fig. 4) is transferred into the third thermal boundary conditions and then applied on the outer surface of the model. A 336-hour heat transfer analysis is conducted for obtaining the time-varying temperature field. Point A (−0.85, −0.35) near the outer surface is selected to calculate the strain.

Fig. 5 (a) shows the sectional temperature field at the 10th hour. T_A, T_{ex} and T_{ey} at any time are calculated according to Eq. (12). The temperature-induced strain of Point A is calculated according to Eq. (13). For comparison, the thermal-induced strain of the FE model is also calculated through the structural analysis and the strain field at the 10th hour is illustrated in Fig. 5 (b). The strain is linearly distributed in the section, which also verifies the plane section assumption.

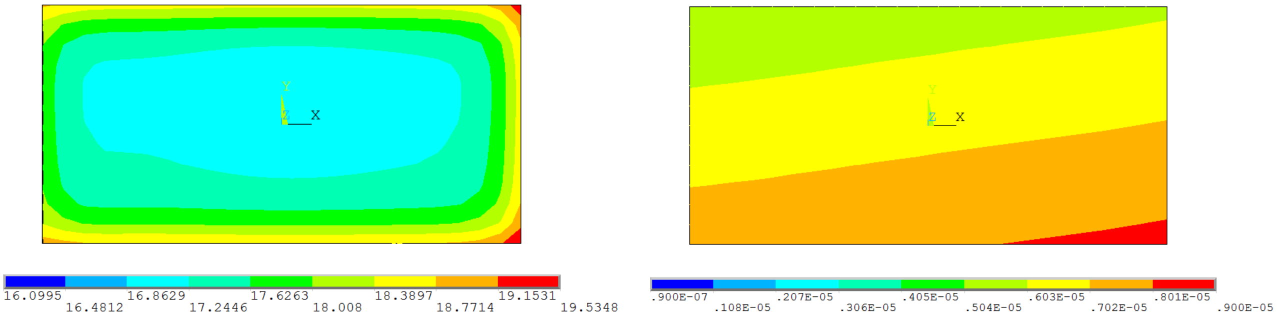

(a) Temperature field

(b) Strain field

Fig. 5. Temperature and strain fields of the column at 10th hours

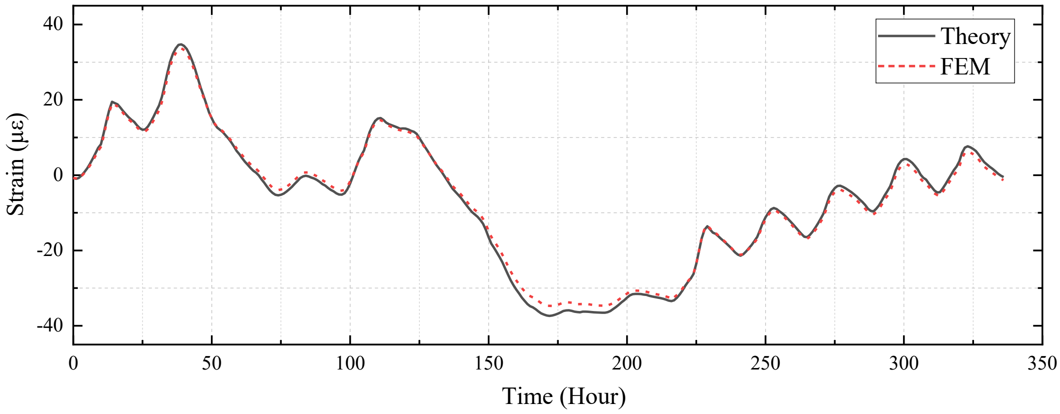

Fig. 6. Comparison between the theoretical and FE numerical strains of point A

The strain time history at Point A calculated from the present theoretical formula and the FE model are compared in Fig. 6. The two curves are very close. Furthermore, the strain field calculated by the

FE model at a certain time is fitted to a plane equation, $\varepsilon = \alpha(c + by + ax)$, where ε represents strain, $\alpha=10\times10^{-6}$/°C is the thermal expansion coefficient, and a, b and c are the fitting coefficients of the plane equation, which are corresponding to T_{ey}, T_{ex} and T_A in Eq. (12). These three pairs of coefficients (c and T_A, b and T_{ex}, and a and T_{ey}) are compared in Fig. 7 and the results are consistent. This verifies that the average surface temperature T_A, the gradient temperature T_{ex} and T_{ey} cause axial strain, y-direction and x-direction gradient strain, respectively.

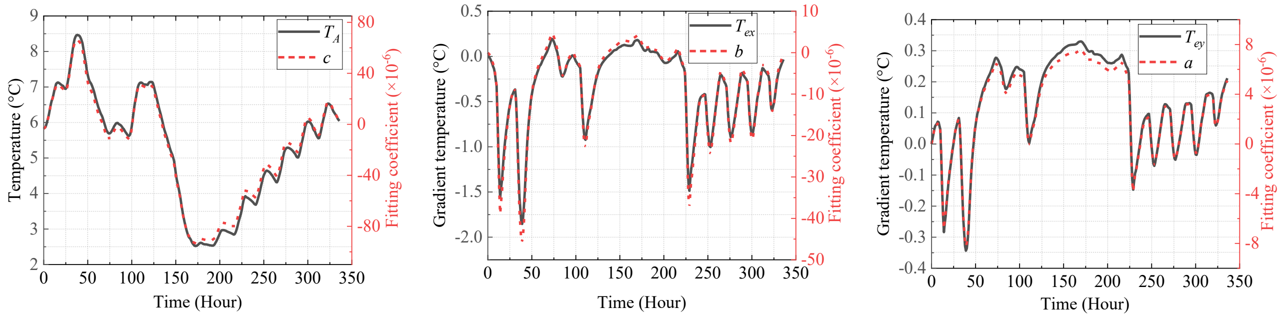

(a) T_A with c (b) T_{ex} with b (c) T_{ey} with a

Fig. 7. Relationship between temperature components and strain fitting coefficients

Table 2. Maximum theoretical contribution ratio of three temperature components

	$T_A=\overline{T}$ (°C)	$T_{ex}=1/2\Delta T_x$ (°C)	$T_{ey}=1/2\Delta T_y$ (°C)	Contribution ratio of T_A	Contribution ratio of T_{ex}	Contribution ratio of T_{ey}
In Spring	10	6	6	45.46%	27.27%	27.27%
In Summer	27	5	5	72.98%	13.51%	13.51%
In Autumn	25	6	6	67.56%	16.22%	16.22%
In Winter	8	5	5	44.44%	27.78%	27.78%

Further, the contribution of T_A, T_{ex} T_{ey} to the total strain is different. In general, T_A contributes most to the strain. Consider the simplest possible situation: $k_1 = k_2 = k_3 = 0$ and the temperature field is linearly distributed along the two sectional directions, which are ΔT_x and ΔT_y, respectively. The temperature-induced strain formula is simplified to: $\varepsilon(x_0,y_0)=\alpha(T_A+\frac{x}{b_x}\Delta T_x+\frac{y}{b_y}\Delta T_y)$, which b_x and b_y are the sectional heights along the x and y directions, respectively. Table 2 shows the average temperature $\overline{T}$ and maximum temperature difference ΔT in Wuhan in one year. When the strain contribution ratio of T_{ex} and T_{ey} is the largest, $x/b_x=y/b_y=1/2$. The contribution of three temperature components to the strain is shown in Table 2. It can be found that in four different seasons, the minimum contribution of T_A to strain fluctuates between 44.44% and 72.98%, accounting for the largest proportion; the maximum contribution of T_{ex} and T_{ey} to strain fluctuates between 13.51% and 27.78%, accounting for the smaller proportion; When the average temperature decreases or the temperature difference increases, the contribution of T_{ex} and T_{ey} increases; conversely, the contribution of T_A increases. In this FE example, Fig. 8 illustrates the three components during the 336 hours period. T_A contributes more than 90% to the strain. The ratio change in Fig.8 meets the above rules.

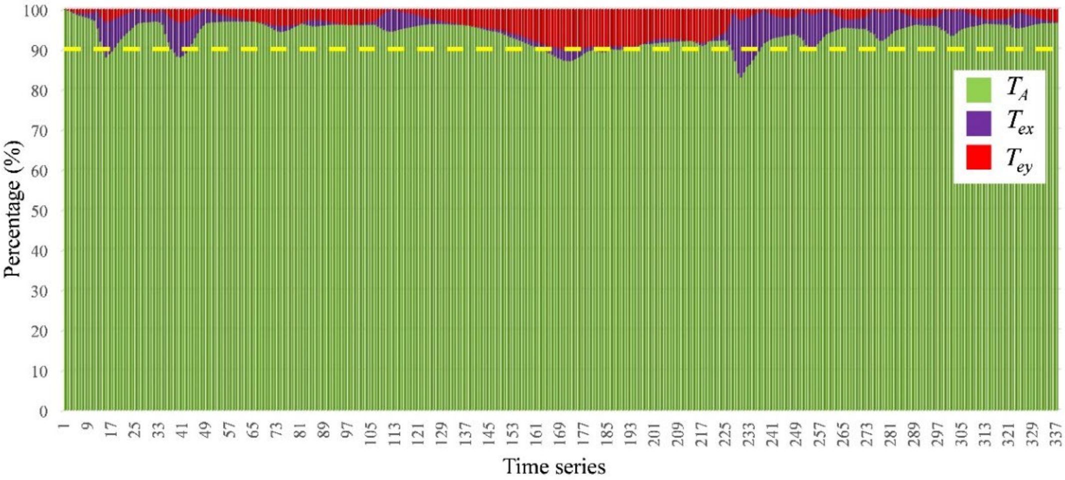

Fig. 8. Contribution of T_A, T_{ex}, T_{ey} to the total strain

5. Case study: a supertall structure

5.1. Wuhan Yangtze River Navigation Centre and its SHM system

The proposed strain calculation is applied to the newly completed Wuhan Yangtze River Navigation Centre, a supertall frame-tube structure with a total height of 335 m as illustrated in Fig. 9(a). This building consists of a 66-floor square main body and a triangular steel roof. During the construction stage, the outer frames and inner core tube were constructed simultaneously.

Fig. 9 (b) shows the typical floor of this skyscraper. The floor section has a constant size of 50.6 m × 50.6 m, surrounded by 20 columns consisting of 4 concrete-filled tube (CFT) columns at the corners and 16 square steel-reinforced concrete (SRC) columns in the middle of each facade. The inner core tube is a square with the dimensions of 30.0 m × 30.0 m. The core tube and the columns are connected through concrete beams.

A long-term SHM system has been installed on the structure to monitor the structural performance during both construction and service stages. Six monitoring sections have been selected along the height for temperature and strain monitoring. These monitoring sections are located on the 10th, 18th, 28th, 38th, 48th and 58th storeys, which correspond to the heights of 47.05, 83.05, 129.55, 176.05, 222.55 and 265.05 m, respectively. A weather station was deployed near the skyscraper to record the surrounding meteorological parameters, such as environmental temperature, wind speed, solar radiation, etc.

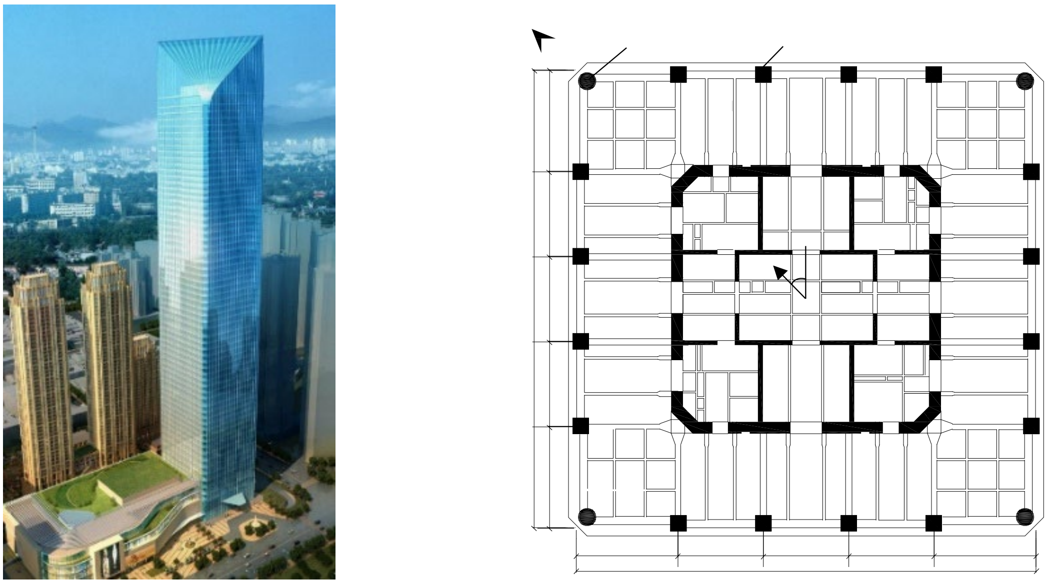

(a) Perspective view

(b) A typical floor of the structure

Fig. 9. Wuhan Yangtze River Navigation Centre

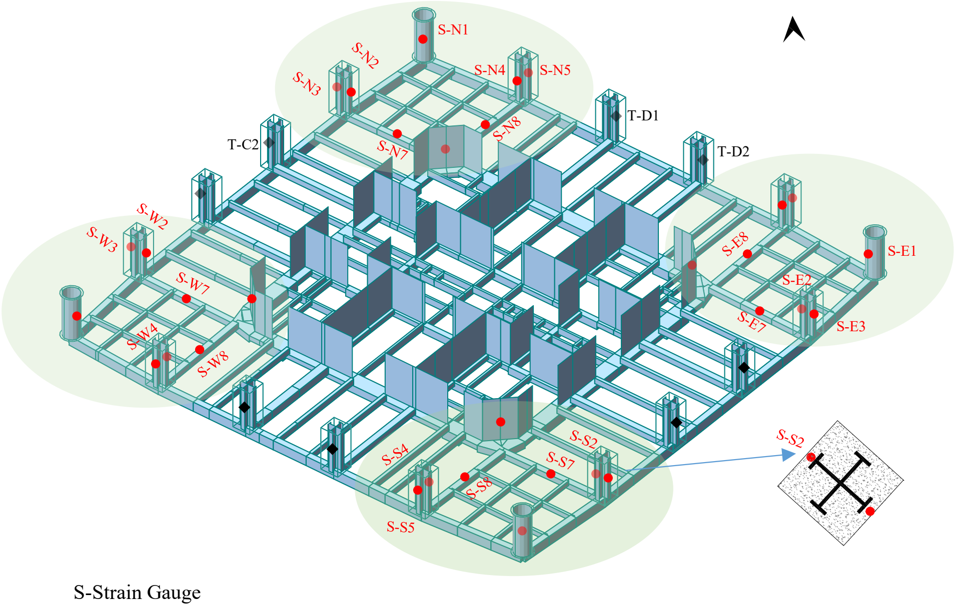

Fig. 10. Sensor layout of a typical monitoring section

All six monitoring sections have the same sensor layout. As shown in Fig. 10, a typical monitoring sections consists of 32 vibrating wire strain gauges and eight temperature sensors. The strain gauges are distributed in the east, south, west and north zones. For example, in the east zone, one strain gauge is installed in the CFT column, named S-E1 (‘S’ represents ‘strain’, and ‘E’ is for ‘east’), four in the SRC columns (named S-E2 to S-E5), one in the core tube (S-E6) and two in the beams (named S-E7 and S-E8). The vibrating wire strain gauges can measure the strain and temperature of one point simultaneously. The temperature sensors are installed in the eight middle SRC columns, denoted as T-A1 and T-A2 to T-D1 and T-D2. All strain gauges and temperature sensors are embedded in the concrete 60 mm from the surface. The sampling rate of the strain gauges and temperature sensors is one reading per 10 min.

5.2. The FE model

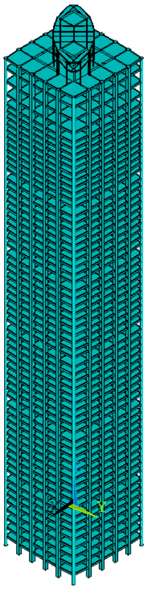

(a) Entire solid model

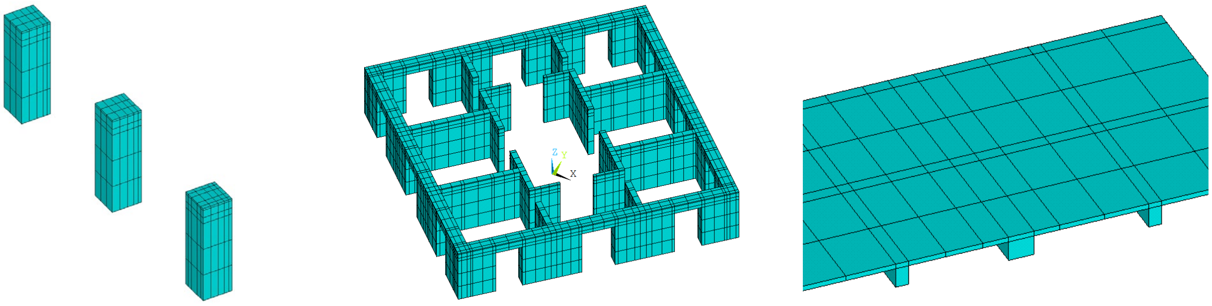

(b) Columns (c) Core tube (d) Beams and slabs

Fig. 11. The FE model of Wuhan Yangtze River Navigation Centre

An FE model is established according to the actual geometry of the structure on the ANSYS platform, as shown in Fig. 11. Given that the steel bars are embedded in the concrete and their cross-sectional area is only approximately a tenth of the total section, the effect of the steel bars on the concrete temperature field can be neglected. Therefore, only concrete is included in the FE model. The element type Solid90 is used for all elements, each consisting of 20 nodes with one thermal DOF at each node. The element mesh sizes of the columns, core tube, beams and slabs are approximately 0.12, 0.20, 0.48 and 0.6 m, respectively. The mass density of the material is 2635 kg/m^3. The equivalent elastic modulus of columns, core tube, beams and slabs are 3.7×10^{10}, 4.44×10^{10}, 3.33×10^{10} and 3.07×10^{10} N/m^2, respectively. The thermal expansion coefficient is 10×10^{-6}/°C. Only temperature load is considered in the FE model.

5.3. Simulation of time-varying temperature field

The monitoring data from November 18 to December 16, 2017 were selected for the heat transfer analysis. During this period, the structure was constructed on the 28th floor. The FE model at this construction stage is released from the entire model. The meteorological data recorded from the weather station are shown in Fig. 12. The virtual sun method is conducted to obtain the time-varying temperature field during this period. Points T18-E3, T18-S4, T18-W3 and T18-N4 at four different directions are selected for comparison, as shown in Fig. 13.

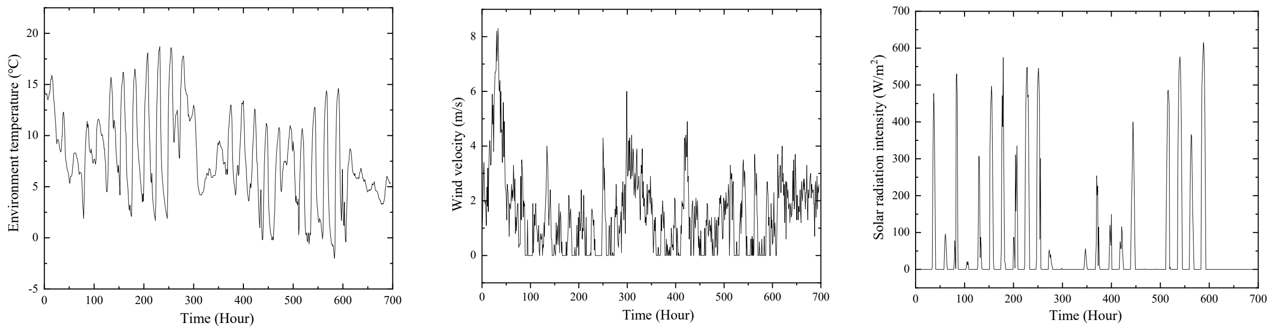

(a) Environment temperature (b) Average wind velocity (c) Solar radiation intensity

Fig. 12. Meteorological data from November 18, 2017 to December 16, 2017

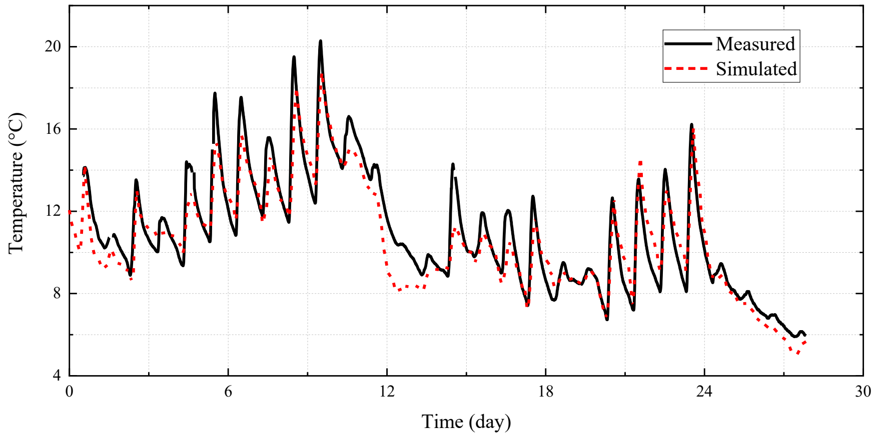

(a) East point T18-E3

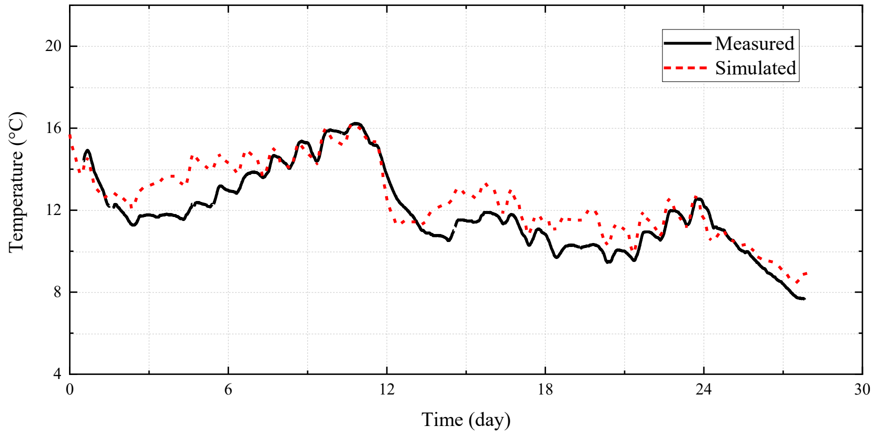

(b) South point T18-S4

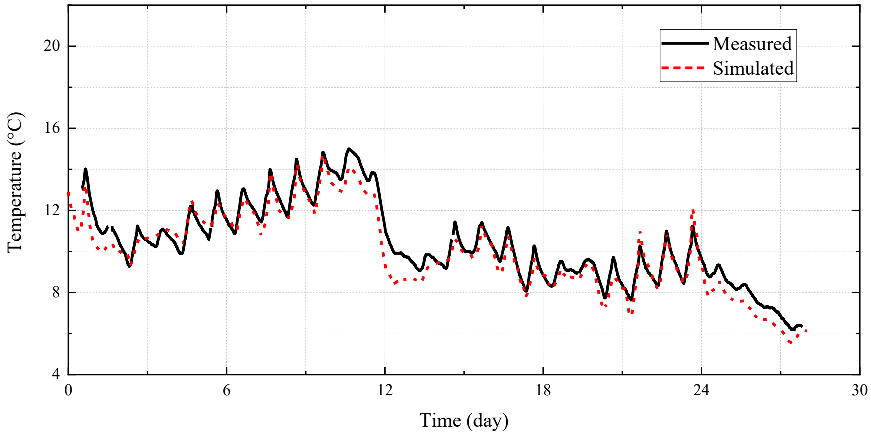

(c) West point T18-W3

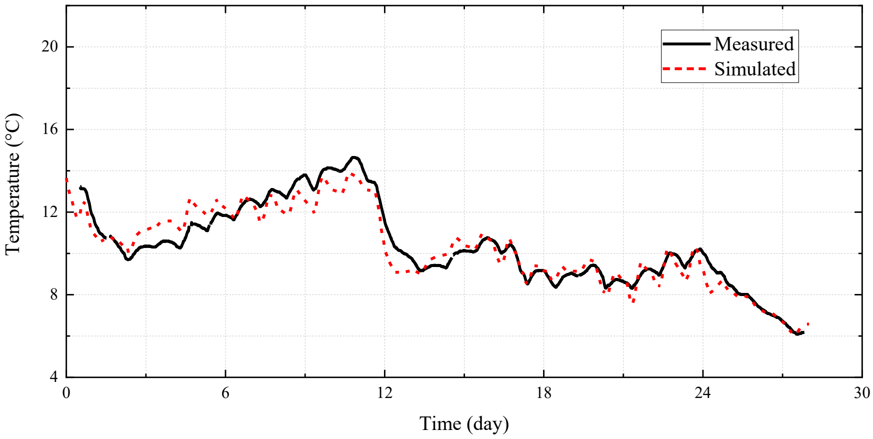

(d) North point T18-N4

Fig. 13. Verification of the simulated temperature field

The root mean square difference (*RMSD*) between the simulated and measured temperature are calculated by

$$RMSD = \sqrt{\frac{1}{n}\sum_{i=1}^{n}(T_s - T_m)^2}\,, \tag{14}$$

where n represents the number of measured points; T_s and T_m denote the simulated temperature and measured temperature, respectively. The relative root mean square difference (*RRMSD*) between the simulated and measured temperature are calculated by

$$RRMSD = \frac{RMSD}{T_{\max} - T_{\min}}\,, \tag{15}$$

where T_{max} and T_{min} represents the maximum temperature and minimum temperature in the measured temperature, respectively; *RRMSD* indicates the relative difference between simulated and calculated temperatures.

The *RMSD* and *RRMSD* of these four points are listed in Table 3. The maximum *RMSD* and *RRMSD* in these four points are 1.03 °C and 11.63%, respectively. The average *RMSD* and *RRMSD* in these four points are only 0.81 °C and 8.18%, respectively. The simulated temperature field agrees well with the calculated temperatures, which will be used for the calculation of the temperature-induced strain.

Table 3. The *RMSD* and *RRMSD* between the simulated and measured temperature

Point	T18-E3	T18-S4	T18-W3	T18-N4	Average
RMSD/°C	1.03	1.00	0.62	0.59	0.81
RRMSD	7.16%	11.63%	7.03%	6.89%	8.18%

5.4. Theoretical estimation of temperature-induced strain

The structural temperature field at any time can be obtained through the FE simulation. The temperature-induced strain of the structural component is then calculated by using Eqs. (11) to (13).

For example, for the column where the measuring point S18-E3 is located, the parameters in Eq. (11) are determined as follows: $\int T(x,y)dA$, $\int T(x,y)ydA$ and $\int T(x,y)xdA$ are calculated by the simulated temperature field; H is the storey height; $A = 3.24$ m^2 is the area of the column section; $E = 3.7\times10^{10}$ N/m^2; $I_x = I_y = 0.87$ m^4 are the x-direction and y-direction moments of inertia; k_1, k_2 and k_3 represent axial spring stiffness, x- and y-direction rotation stiffness and are caused by the surrounding beams and slabs. In a real structure, k_1, k_2 and k_3 are difficult to calculate. As Fig. 10 demonstrates, T_A contribute most to the strain. Therefore, Eq. (11) is simplified as

$$\varepsilon \approx \alpha \frac{\int T(x,y)dA}{\frac{k_1 H}{E}+A} = C\int T(x,y)dA, \tag{16}$$

where $C = \alpha/(k_1H/E+A)$ is a constant. The above formula reveals that the strain is approximately proportional to $\int T(x, y)dA$, which are available from the FE heat transfer analysis. Eq. (16) can be used to estimate the temperature-induced strain in a real structure. The calculated time–history strain the structure is compared with the measured one in Fig. 14.

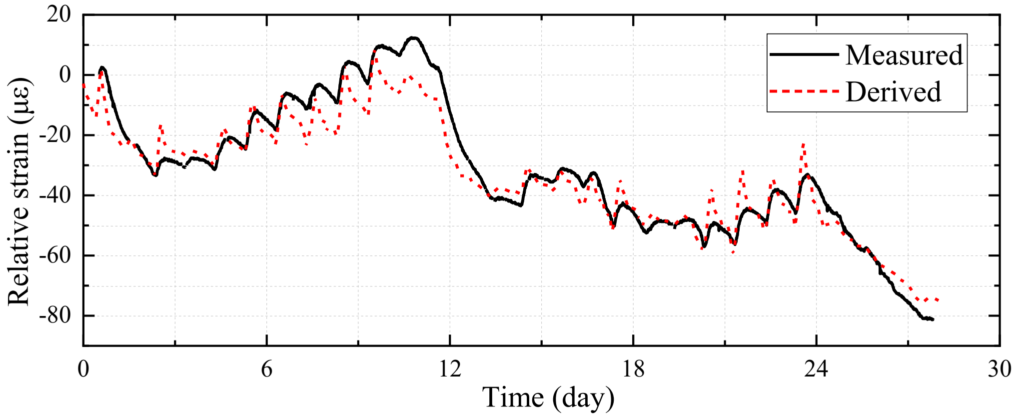

Fig. 14. The derived and measured strain

Fig. 14 shows that the derived strain reflects the fluctuation and trend of the strain successfully. The *RMSD* and *RRMSD* between the derived and measured strain are 6.18 με and 6.6%, respectively. The difference between the two curves is mainly caused by three reasons: First, the simulated temperature field has errors with the actual temperature field. Second, the measured strain includes not only temperature strain but also those due to the construction load, concrete shrinkage, concrete creep and wind load. Third, the temperature-induced strain caused by gradient temperature is reduced in Eq. (16). Nevertheless, the small difference indicates that the temperature-induced strain dominates the total strain of the structure in practice.

The method proposed in this paper provides a new method for estimating the temperature-induced strain in field monitoring without the FE structural analysis. The mechanism between temperature and strain is detailed described. The structural response due to other loads can be subsequently obtained by subtracting the pure temperature-induced strain from the measured total strain.

6. Conclusions

In this paper, the temperature-strain formula is derived through the mapping relationship between the temperature field and strain. A generalised cantilever column FE model verifies the correctness of the temperature-strain formula. Taking the Wuhan Yangtze River Navigation Centre as the test bed, the temperature-induced strain was successfully estimated by a combination of FE heat transfer analysis and temperature-strain formula. The following conclusions are drawn.

(1) Simplifying the bending-mode supertall structure into a generalised cantilever column is feasible when deriving the temperature-induced strain.

(2) The temperature-induced strain for the columns or the core tube of a supertall structure is composed of three parts: the sectional average temperature-induced strain, the x-direction gradient temperature-induced strain and the y-direction gradient temperature-induced strain. The sectional average temperature contributes most to the strain.

(3) The measured strain fluctuates every day, which is mainly caused by temperature variations. Combining the FE heat transfer analysis and the temperature-strain formula derived in this paper, we can estimate the temperature-induced strain. The RMSE of the derived and measured strain is within 7 με.

Acknowledgements

This work is supported by grants from the National Natural Science Foundation of China (NSFC, Project No. 51978308, 51629801 and 51922046), the Projects of Strategic Importance of The Hong Kong Polytechnic University (Project No. 1-ZE1F) and the Research Grants Council of the Hong Kong Special Administrative Region, China(Project No. PolyU 152621/16E).

References

[1] Sony S, Laventure S, Sadhu A. A literature review of next‑generation smart sensing technology in structural health monitoring[J]. Structural Control and Health Monitoring, 2019, 26(3): e2321.

[2] Li H N, Ren L, Jia Z G, et al. State-of-the-art in structural health monitoring of large and complex civil infrastructures[J]. Journal of Civil Structural Health Monitoring, 2016, 6(1): 3-16.

[3] Zhou J, Li X, Xia R, et al. Health monitoring and evaluation of long-span bridges based on sensing and data analysis: A survey[J]. Sensors, 2017, 17(3): 603.

[4] Zhou Y, Sun L. A comprehensive study of the thermal response of a long-span cable-stayed bridge: From monitoring phenomena to underlying mechanisms[J]. Mechanical Systems and Signal Processing, 2019, 124: 330-348.

[5] Yang D H, Yi T H, Li H N, et al. Monitoring and analysis of thermal effect on tower displacement in cable-stayed bridge[J]. Measurement, 2018, 115: 249-257.

[6] Su J Z, Xia Y, Weng S. Review on field monitoring of high-rise structures[J]. Structural Control and Health Monitoring, 2020, 27(12): e2629.

[7] Xia Y, Ni Y Q, Zhang P, et al. Stress development of a supertall structure during construction: Field monitoring and numerical analysis[J]. Computer-Aided Civil and Infrastructure Engineering, 2011, 26(7): 542-559.

[8] Ni Y Q, Li B, Lam K H, et al. In-construction vibration monitoring of a super-tall structure using a long-range wireless sensing system[J]. Smart Structures and Systems, 2011, 7(2): 83-102.

[9] Su J Z, Xia Y, Chen L, et al. Long-term structural performance monitoring system for the Shanghai Tower[J]. Journal of Civil Structural Health Monitoring, 2013, 3(1): 49-61.

[10] Zhang F L, Yang Y P, Xiong H B, et al. Structural health monitoring of a 250-m super-tall building and operational modal analysis using the fast Bayesian FFT method[J]. Structural Control and Health Monitoring, 2019: e2383.

[11] Liu T, Yang B, Zhang Q. Health monitoring system developed for Tianjin 117 high-rise building[J]. Journal of Aerospace Engineering, 2016, 30(2): B4016004.

[12] Russel H G, Larson S C. Thirteen years of deformations in water tower place[J]. Structural Journal, 1989, 86 (2): 182-191.

[13] Brownjohn J, Pan T C, Deng X. Correlating dynamic characteristics from field measurements and numerical analysis of a high-rise building[J]. Earthquake Engineering & Structural Dynamics, 2000, 29 (4): 523-543.

[14] Celebi M, Sanli A. GPS in pioneering dynamic monitoring of long-period structures[J]. Earthquake Spectra, 2002, 18(1): 47-61.

[15] Tamura Y, Matsui M, Pagnini L C, et al. Measurement of wind-induced response of buildings using

RTK-GPS[J]. Journal of Wind Engineering & Industrial Aerodynamics, 2002, 90 (12): 1783-1793.

[16] Breuer P, Chmielewski T, Górski P, et al. The Stuttgart TV Tower – displacement of the top caused by the effects of sun and wind[J]. Engineering Structures, 2008, 30 (10): 2771-2781.

[17] Xia Y, Zhang P, Ni Y Q, et al. Deformation monitoring of a super-tall structure using real-time strain data[J]. Engineering Structures, 2014, 67: 29-38.

[18] Su J Z, Xia Y, Ni Y Q, et al. Field monitoring and numerical simulation of the thermal actions of a supertall structure[J]. Structural Control and Health Monitoring, 2017, 24(4): e1900.

[19] Zhang P. Field monitoring and numerical analysis of temperature effects on a super-tall structure[D]. The Hong Kong Polytechnic University, 2016.

[20] Su J Z, Xia Y, Zhu L D, et al. Typhoon- and temperature-induced quasi-static responses of a supertall structure[J]. Engineering Structures, 2017, 143: 91-100.

[21] Zhu Y, Ni Y Q, Jesus A, et al. Thermal strain extraction methodologies for bridge structural condition assessment[J]. Smart Materials and Structures, 2018, 27(10): 105051.

[22] Yang K, Ding Y, Sun P, et al. Modeling of temperature time-lag effect for concrete box-girder bridges[J]. Applied Sciences, 2019, 9(16): 3255.

[23] Ni Y Q, Zhang P, Ye X W, et al. Modeling of temperature distribution in a reinforced concrete supertall structure based on structural health monitoring data[J]. Computers & Concrete, 2011, 8(3): 293-309.

[24] Su J Z. Construction settlement monitoring and thermal actions monitoring of supertall structures[D]. The Hong Kong Polytechnic University, 2015.

[25] Gao F, Chen P, Xia Y, et al. Efficient calculation and monitoring of temperature actions on supertall structures[J]. Engineering Structures, 2019, 193: 1-11.

[26] Hu Y, Hou R, Xia Q, et al. Temperature-induced displacement of supertall structures: A case study[J]. Advances in Structural Engineering, 2019, 22(4): 982-996.

[27] Bai X, Yang N, Yang Q. Temperature effect on the structural strains of an ancient Tibetan building based on long-term monitoring data[J]. Earthquake Engineering and Engineering Vibration, 2018, 17(3): 641-657.

[28] Yang N, Bai X. Forecasting structural strains from long-term monitoring data of a traditional Tibetan building[J]. Structural Control and Health Monitoring, 2019, 26(1): e2300.

[29] Ã–zisik M N, Özısık M N, Özışk M N. Heat conduction[M]. John Wiley & Sons, 1993.

[30] Zhou L, Xia Y, Brownjohn J M W, et al. Temperature analysis of a long-span suspension bridge based on field monitoring and numerical simulation[J]. Journal of Bridge Engineering, 2015, 21(1): 04015027.

[31] Cohen M F, Greenberg D P. The hemi-cube: A radiosity solution for complex environments[J]. ACM Siggraph Computer Graphics, 1985, 19(3): 31-40.